P. Brambilla, P. Brivio, A. Guardone, G. Romanelli
Grid Convergence Assessment for Adaptive Grid Simulations of Normal Drop Impacts onto Liquid Films in Axi-Symmetric and Three-Dimensional Geometries
Applied Mathematics and Computation, Vol. 267, 2015, p. 487-497
doi:10.1016/j.amc.2015.01.097

Grid convergence assessment for adaptive grid simulations of normal drop impacts onto liquid films in axi-symmetric and three-dimensional geometries

P. Brambilla, P. Brivio, A. Guardone *

Department of Aerospace Science and Technology, Politecnico di Milano via La Masa, 34, 20156 Milano, Italy

G. Romanelli

Competence Center Fluid Mechanics and Hydrolic Machines Lucerne University of Applied Sciences and Arts, Technikumstrasse 21 6048 Horw, Lucerne, Switzerland

Abstract

Normal liquid drop impact on a liquid film is studied numerically using a modified OpenFOAM solver in three-spatial dimensions, in which dynamic grid refinement is modified to accurately describe the initial conditions before impact. Numerical simulations are found to accurately predict the evolution of the splashing lamella. A new procedure for assessing grid convergence is introduced, which is based on the definition of a hierarchical set of bounding boxes in which the total liquid volume is computed to assess global as well as local grid convergence.

Key words: Drop impact dynamics, two-phase flow, dynamic grid refinement, OpenFOAM

1 Introduction

The understanding of drop impact dynamics is of paramount importance in numerous technical applications and in the study of natural phenomena. Ink-jet printing, internal combustion engines and soil erosion are examples. Even

* Corresponding author
Email address: `alberto.guardone@polimi.it` (A. Guardone).

for the simplest case of drop with a trajectory normal to the wall impacting on a liquid film, drop impact dynamics and splashing is far from being understood both because of its complexity and the large number of parameters which influence it. These are e.g. the Weber, Ohnesorge and Reynolds numbers, which are dimensionless groups whose numerical value depends on the drop velocity, density, superficial tension, dynamic viscosity and size. With reference to figure 1, the evolution of the splash generated by the impacting drop is characterized by crown formation (figure 1(a)), rim instability (figure 1(b)), formation and eventual break-up of jets resulting in secondary droplets (figure 1(c)) and collapse of the crown (figure 1(d)), see also [16,7,10]. Oblique impacts are investigated in [9].

Weiss and Yarin [17] carried out a numerical analysis of drop impact on thin liquid films. They investigated normal impacts resulting in axisymmetric flow structures by using a potential boundary-integral method. They found that shortly after impact, a disk-like jet forms at the neck between the drop and the liquid film if the Weber number is high enough. For larger times after impact, the authors compared their results with the theoretical predictions of the quasi-one-dimensional model of Yarin and Weiss [18] and they found a good agreement in terms of the time evolution of the crown radius. Similarly to the work of Weiss and Yarin, in 2003 Josserand and Zaleski [6] focused on the initial stages after impact. The authors solved the axisymmetric incompressible Navier-Stokes equations with surface tension written in the one-fluid formulation. Their results show that the width of the ejected liquid sheet during impact is controlled by a viscous length. This theory agrees with the experiments reported by Thoroddsen [15]. Purvis and Smith [11] and later Quero et al.[12] dealt with Super Large Droplets (SLD) impacting on a thin water layer. The simulations resorted to a two-dimensional approximation and were compared to experiments performed under similar conditions. A thermal model was also included in order to predict the ice growth for aircraft icing applications. Rieber and Frohn [13] in 1999 and Nikolopoulos et al. [8] in 2007 presented a three-dimensional numerical investigation of a droplet impinging normally on a liquid film, the latters considering the effect of the gravitational field. In both papers drop impacts were simulated with the same Weber number. In [13], random disturbances were added to the flow to trigger flow instabilities. The numerical method was based on the finite volume solution of the Navier-Stokes equations coupled with the Volume-of-Fluid (VOF) method. An adaptive local grid refinement technique for tracking more accurately the liquid-gas interface was used in [8].

In this work we perform accurate numerical simulations of normal drop impacts on a thin liquid film. We solve the Navier-Stokes equations for incompressible fluids in three-dimensions using a dynamic grid refinement technique. We use two-phase solvers implemented in the open-source software OpenFOAM modified by the us to allow for an accurate representation of the initial solution.

The next section reports briefly on the numerical method and its implementation in OpenFOAM. In the third section the numerical simulations are described and the results are compared with theoretical predictions; a new procedure for assessing grid convergence is also introduced. One of the experiments reported in literature is numerically reproduced and a comparison between numerical and experimental results is presented. The paper ends with concluding remarks.

2 Volume-Of-Fluid method for multi-phase flows

Currently three main approaches are used to tackle multi-phase flows. The first one is the Euler-Lagrange model which assumes that the topology of the two-phase flow is dispersed. The two phases are therefore referred to as the continuous and the dispersed phase. Another approach is the Euler-Euler model which solves the averaged Eulerian conservation equations for laminar flows. In this case, the topology of the interface is the outcome of the solution and it can be marked by free-surface methodologies. The latter can be classified into:

- surface tracking methods: where a sharp interface is defined whose motion is tracked in time;
- moving mesh methods: in which the interface is associated to a set of nodal points of the computational mesh;
- volume tracking methods: in this case, the interface is not defined as a sharp boundary and the different fluids are marked by an indicator function.

More details on the Euler-Lagrangian and Euler-Euler methods can be found in H. Rusche's work [14].

In the present work, we use the Euler-Euler approach coupled to the volume tracking method. In particular, we use the Volume-Of-Fluid (VOF) method by Hirt and Nichols [3], in which the indicator function is the volume fraction of the dispersed phase denoted with α. The fluids are assumed to be newtonian, incompressible and immiscible. Therefore we do not take into account thermal and mass exchanges between the phases. The Navier-Stokes equations written in the one-fluid formulation are

$$\nabla \cdot \vec{V} = 0 \tag{1a}$$

$$\frac{\partial \rho \vec{V}}{\partial t} + \nabla \cdot (\rho \vec{V}\vec{V}) = -\nabla p + \nabla \cdot \Sigma + \rho \vec{f} + \int_{S(t)} \sigma k' \vec{n'} \delta(x - x') dS \tag{1b}$$

where $\vec{V}$ is the velocity field, ρ is the density, p is the pressure, $\vec{f}$ is the acceleration due to the volume forces, $\Sigma = \mu(\nabla \vec{V} + \nabla \vec{V}^T)$ is the stress tensor, σ is the superficial tension coefficient, k is the surface curvature and $\vec{n}$ is the local normal. The last term of the momentum equation accounts for the superficial tension. Density and viscosity are constant inside the two fluids, but vary discontinuously at the sharp interface. In the VOF method the two properties are related to the volume fraction α by

$$\rho = \alpha\rho_a + (1-\alpha)\rho_b \tag{2}$$

$$\mu = \alpha\mu_a + (1-\alpha)\mu_b \tag{3}$$

The volume fraction α assumes the following values

$$\alpha = \begin{cases} 1 & \text{if the cell is completely full of liquid} \\ 0 < \alpha < 1 & \text{if the cell contains the interface} \\ 0 & \text{if the cell is completely full of gas} \end{cases} \tag{4}$$

Advection of the liquid volume, and thus of the discontinuity, is governed by the transport equation

$$\frac{\partial \alpha}{\partial t} + \nabla \cdot (\vec{V}\alpha) = 0 \tag{5}$$

There are some numerical difficulties in modeling surface tension effects because the interface is not a sharp boundary. Hence we use the Continuum Surface Force (CSF) model (Brackbill et al. [1]) which interprets surface tension as a continuous, three-dimensional effect across an interface.

2.1 VOF implementation in OpenFOAM

In OpenFOAM the VOF method is implemented by the *interFoam* solver. We use the *blockMesh* dictionary included in OpenFOAM to generate the mesh. For the purpose of applying boundary conditions, a boundary is generally broken up into a set of *patches*. One patch may include one or more enclosed areas of the boundary surface which do not necessarily need to be physically connected. The setting of a non-uniform initial condition, such as for the phase fraction α in this case, is done by running the *setFields* utility. The *fvSchemes* dictionary is defined as follows:

- time derivative: first order implicit backward Euler scheme;
- gradient: second order, Gaussian integration with linear interpolation;
- avection term of the momentum equation: second order, Gaussian integration with limited linear differencing scheme for vector fields;

- advection of the volume fraction α: second order, Gaussian integration with van Leer limiter scheme;
- advection of the volume fraction α due to the velocity field $\vec{V}_{rb}$: second order, Gaussian integration with the so-called *interfaceCompression* scheme which produces a sharp interface;
- laplacian term: second order, Gaussian integration with linear interpolation for the viscosity function and with explicit non-orthogonal correction scheme for surface normal gradient of the velocity field;
- interpolation schemes: linear interpolation;
- surface normal gradient: explicit non-orthogonal correction scheme.

In all computation, the Courant-Friedrichs-Lewy (CFL) number is set equal to 0.3. Note that the default CFL number suggested by the OpenFOAM documentation is 0.5 for cases where a surface-tracking algorithm is used.

The dynamic grid refinement technique is implemented in the solver according to Jasak's and Jasak and Gosman's h-refinement approaches [4,5]. The computational grid is locally refined if the cell value of α is larger than 0 and lower than 1. New computational nodes are inserted in the cells marked for refinement. The maximum refinement level, that is the maximum number of subdivisions of the initial cells, can be set. At each refinement step, each cell edge is divided into two new edges in the x, y and z direction, which in turns define 16 new elements within the old cell. Unfortunately, the in the solver the initial condition can be assigned only over the initial, namely, not refined, grid, which does not allow for a sharp representation of the drop boundaries, as shown in figure 2. To circumvent this limitation, a new procedure is included in the solver which allows to apply initial conditions after few refinement cycles as follows. During the first five refinement steps the value of α is assumed to be 0.9 in the liquid film to force grid refinement at the liquid-gas interface. At the sixth (and last) refinement step the value of α in the liquid phase is set back to 1. Then, the time is set back to zero and the initial conditions are imposed on the new refined grid. Figure 3 shows the improvements obtained using the modified solver.

Numerical experiments where carried out on a Linux cluster with 16 computational nodes, each equipped with two six-core Xeon 2.66 GHz CPU and 32 GB RAM. The typical simulation in the S geometry (see below) with four refinement levels required approximately 110 hours on 4 cores and 37 hours on 16 cores. Further reduction of the computational time were found to be impractical because of the poor scaling due to a lack of a load balancing technique within the dynamic mesh solver.

3 Drop impact simulations

Two normal drop impact problems from reference [13] are presented. Case A corresponds to a Weber number $\mathrm{We}_\mathrm{A} = 250$, where the Weber number We is defined as $\mathrm{We} = (\rho_d D * V_\mathrm{d}^2)/\sigma$, with ρ_d liquid density, D drop diameter, V_d drop velocity and σ surface tension. In case C, $We_\mathrm{C} = 598$. In both cases A and C, the film thickness is made dimensionless by D is 0.116 and the Ohnesorge number Oh, $\mathrm{Oh} = \mu_d/\sqrt{\rho_d \sigma D}$ is 0.0014, with μ_d viscosity of the liquid. For $\mathrm{Oh} = 0.0014$, the critical Weber number is 171 and therefore all considered cases are above the splash threshold.

The wall is located at $y = 0$ and only the $x > 0, y > 0, z > 0$ quadrant is considered. We consider two computational domains. The first corresponds to a cube with an edge of $2.3D$ (S geometry, used in [13]), the second corresponds to a cube with an edge of $3.98D$ (L geometry, used in [8]). The base grid consists of $20 \times 20 \times 20$ cells in both the S and L geometries. We use 2, 3 and 4 levels of refinement. Using the S geometry the maximum resolutions are $2.3D/20/4 = 28.75D \times 10^{-3}$, $2.3D/20/8 = 14.375D \times 10^{-3}$ and $2.3D/20/16 = 7.1875D \times 10^{-3}$, respectively. Using the L geometry the maximum resolutions are $3.98D/20/4 = 49.75D \times 10^{-3}$, $3.98D/20/8 = 24.875D \times 10^{-3}$ and $3.98D/20/16 = 12.4375D \times 10^{-3}$, respectively. The simulation starts with the center of the spherical drop located at $y = 1.5D$ and ends at the dimensionless time $\tau = tV/D = 3.5$ and at $\tau = tV/D = 10$, for the S and L domain, respectively. Figures 4 and 5 show the computed liquid-gas interface for case A and case C, respectively, for the S geometry. The free surface profile along the section $z = x$ are shown in figures 6 for the S domain and the L domain, respectively, and for the three considered refinement levels. Inspection of figure 6 reveals an adequate grid-independence, with all the major flow structure being represented with increasing accuracy.

A more quantitative method for assessing grid convergence is now proposed. The domain is subdivided into nine bounding boxes, three in the radial direction and three in the normal direction. Each bounding box is identified by two integer numbers: the former refers to an uniform subdivision in the radial direction, the latter refers to an uniform subdivision in the normal direction. Each bounding box contains all boxes with lower indexes, i.e. the bounding box number (3,3) contains all the others and the whole liquid volume. In figure 7, bounding box (1,2) is shown in exemplary pre- and post-impact conditions. The plots in figures 8 and 9 show the percentage of the liquid volume inside a given box as a function of time for the S geometry and L geometry, respectively. Refinement 3 and 4 show overlapping results. In case A, refinement 2 is clearly not sufficient, while in case C all the resolutions provides comparable results. Note that case C is associated to at a larger value of the Weber number which results in a wider and higher corona. With particular reference to bounding box (3,1) and (3,2), which are at the top right and middle right of the symmetry plane, in case A a higher refinement can catch little secondary droplets which lower refinement level can not. In case C a major quantity of liquid is located in these bounding boxes therefore both higher and coarser meshes can accurately catch secondary droplets.

A comparison between numerical results of the present paper and those of Rieber and Frohn [13] and Nikolopoulos et al [8] is reported. Figure 10 shows the geometrical quantities considered in the comparison. The height of the crown is marked with the letter H and it is defined as the distance between the liquid film and the maximum height of the rim. The diameter reported for the experimental results is the arithmetic mean of the outer (D_{ou}) and the inner (D_{in}) diameter. Figures 11 and 12 report the comparison of the present simulations against the numerical results presented by Rieber and Frohn [13] and Nikolopoulos et al [8], for the corona radius and height, respectively, as a function of time. The radius of the crown is defined as the radial position of the center of mass of the liquid volume above the liquid film. Figures 11(a), 11(c), 12(a) and 12(c) refer to results on the S geometry, which allows for a maximum elapsed simulation dimensionless time of 3.5, figures 11(b), 11(d), 12(b) and 12(d) refer to results on the L geometry, up to a dimensionless time of 10. The present numerical results are close to those of Nikilopoulos et al., but they differ from those of Rieber and Frohn in particular during the initial evolution of the corona. Note that at $\tau = 1.5$ the droplet is completely impinged on the liquid film. Therefore, for t$\tau < 1.5$, the automatic procedure to detect the radius fails and the calculated value depart from the experimental one. Moreover, in case A, this discrepancy is possibly due to the detachment of a secondary droplet from the rim at $\tau = 1.5$ which results in a larger height at earlier times. In case C, the opposite occurs: a droplet is detaching at earlier time according to Rieber and Frohn's and it does not in the present simulations.

Comparison between figure 12(a) and 12(b) and between figure 12(c) and 12(d) reveals a dependence of the crown height on the considered domain (S or L). Indeed, being smaller in size, the S domain is characterized by a better maximum grid resolution with respect to domain L, which in turns allows representing secondary droplets more accurately. These influence directly the maximum rim height whereas they have a less relevant influence on the rim radius.

To further assess the accuracy of the numerical method, one of the experiments of Cossali et al. [2] was numerically reproduced. Experimental conditions are as follows: $D = 3.82$ mm; $V = 3.0392$ m/s; $H = 0.29$; We=484; Re=11650; Oh=0.0019; K=5934; Ks=3089 . In the simulations of the experiment, the domain is represented by a cube with an edge of $8.5D$ and the resolution is equal to $7.35D \times 10^{-3}$. Figure 13 reports the comparison. Figures 13(a) and 13(b) show the behavior of the outer and inner radius, respectively. All the resolutions are sufficient to describe accurately the radial evolution of the crown. The height detected in the simulation is different from the experiment. This is probably due to the fact that the analysis of the photographs took during the experiment differs from the analysis of the numerical simulation. In fact, in the photographs the free surface is perturbed and it reaches a higher height for effect of the wave generated by the impact. Therefore, the reference surface becomes higher than the unperturbed film.

4 Conclusions

The dynamics of the normal impingement of a drop on a liquid film was numerically studied using an adaptive grid refinement technique. Three-dimensional simulations can accurately predict the evolution of the splashing lamella. A new procedure for assessing grid convergence was introduced, which is based on the definition of a hierarchical set of bounding boxes in which the total liquid volume is computed to assess global as well as local grid convergence. The present results are compared with numerical simulation and experimental results reported in the open literature and the agreement is very good. The differences observed between the present results and the reference ones are possibly due to the difficulty in defining the quantities in a rigorous manner. The present approach can be easily extended to the study of drop impacts with non-normal trajectory.

References

[1] J. U. Brackbill et al. A continuum method for modelling surface tension. *J. of Computational Physics, 100(2):335-354*, 1992.

[2] G. E. Cossali, M. Marengo, A. Coghe, and S. Zhadanov. The role of time in single drop splash on thin film. *Experiments in Fluids, 36:888-900*, 2004.

[3] C. W. Hirt and B. D. Nichols. Volume of fluid (VOF) method for the dynamics of free boundaries. *J. of Computational Physics, 39:201-225*, 1981.

[4] H. Jasak. Error analysis and estimation for the finite volume method with applications to fluid flows. Tesi di Dottorato di Ricerca, Imperial College, University of London, giugno 1996.

[5] H. Jasak and A. D. Gosman. Automatic resolution control for the finite-volume method, part 2: adaptive mesh refinement and coarsening. *Numerical Heat Transfer, part B, 38(3):257-271*, 2000.

[6] C. Josserand and S. Zaleski. Droplet splashing on a thin liquid film. *Physics of Fluids, 15(6):1650-1657*, 2003.

[7] S. Mandre and M. P. Brenner. The making of a splash on a dry solid surface. *J. of Fluid Mechanics, 690:148-172*, 2012.

[8] N. Nikolopoulos et al. Three-dimensional numerical investigation of a droplet impinging normally onto a wall film. *J. of Computational Physics, 225:322-341*, 2007.

[9] T. Okawa, T. Shiraishi, and T. Mori. Effect of impingement angle on the outcome of single water drop impact onto a plane water surface. *Exp Fluids, 44:331-339*, 2008.

[10] K. L. Pan and C. Y. Hung. Droplet impact upon a wet surface with varied fluid and surface properties. *J. of Colloid and Interface Science, 352:186-193*, 2010.

[11] R. Purvis and F. T. Smith. Large droplet impact on water layers. *AIAA Paper 2004-414*, 2004.

[12] M. Quero et al. Analysis of super-cooled water droplet impact on a thin water layer and ice growth. *AIAA Paper 2006-466*, 2006.

[13] M. Rieber and A. Frohn. A numerical study on the mechanism of splashing. *Int. J. of Heat and Fluid Flow, 20:455-461*, 1999.

[14] H. Rusche. *Computational fluid dynamics of dispersed two-phase flows at high phase fraction*. Tesi di Dottorato di Ricerca, Imperial College, University of London, dicembre 2002.

[15] S. T. Thoroddsen. The ejcta sheet generated by the impact of a drop. *J. Fluid Mechanics, 451:373-381*, 2002.

[16] S. T. Thoroddsen. The making of a splash. *J. of Fluid Mechanics, 690:1-4*, 2012.

[17] D. A. Weiss and A. L. Yarin. Single drop impact onto liquid films: neck distortion, jetting, tiny bubble entrainment, and crown formation. *J. of Fluid Mechanics, 385:229-254*, 1999.

[18] A. L. Yarin and D. A. Weiss. Impact of drops on solid surfaces: self-similar capillary waves, and splashing as a new type of kinematic discontinuity. *J. Fluid Mech., 283:141-173*, 1995.

List of Figures

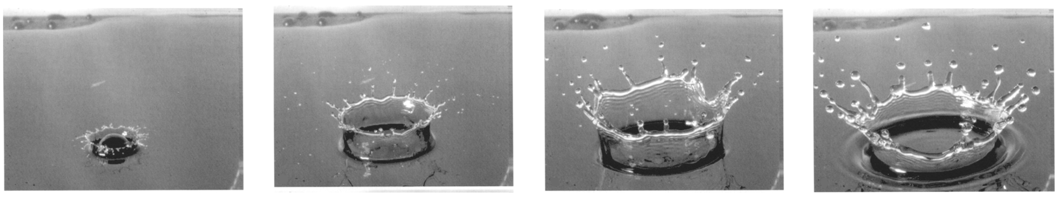

(a) Crown formation (b) Rim instability (c) jet break-up, secondary droplets (d) Collapse of the crown

Fig. 1. Evolution of the splash.

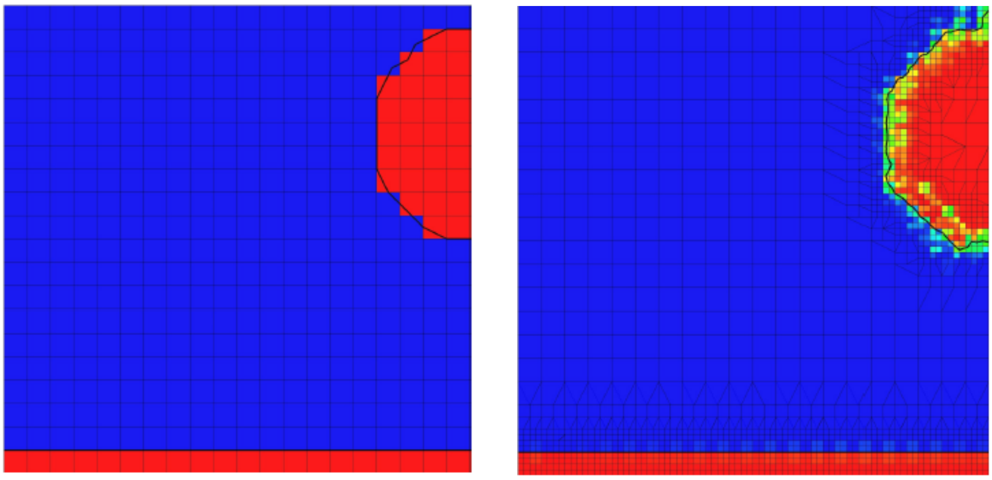

(a)

(b)

Fig. 2. Break-up of the interface: 2(a) initial conditions; 2(b) after first two steps of refinement. Initial grid resolution is $D/10$ and $D/H = 1$.

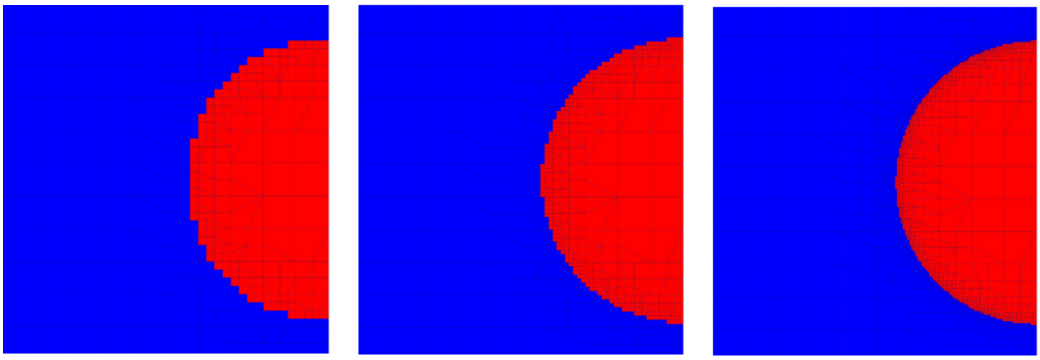

(a) (b) (c)

Fig. 3. Initial time step using the modified solver, contour of the drop: 3(a) two levels of refinement; 3(b) three levels of refinement; 3(c) four levels of refinement. Initial grid resolution is $D/10$ and $D/H = 1$.

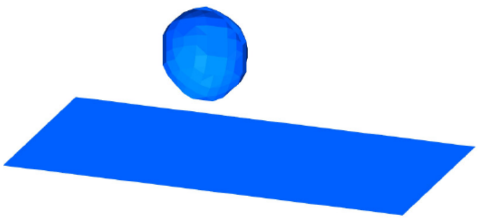

(a) $\tau = -1$

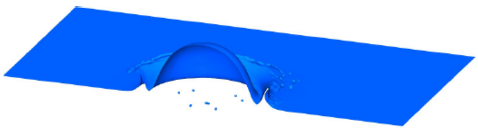

(b) $\tau = 0.45$

(c) $\tau = 1.45$

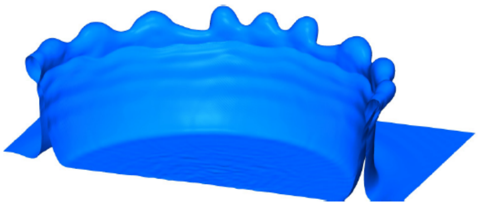

(d) $\tau = 3.7$

Fig. 4. Numerical simulation, case A (Refinement level 4).

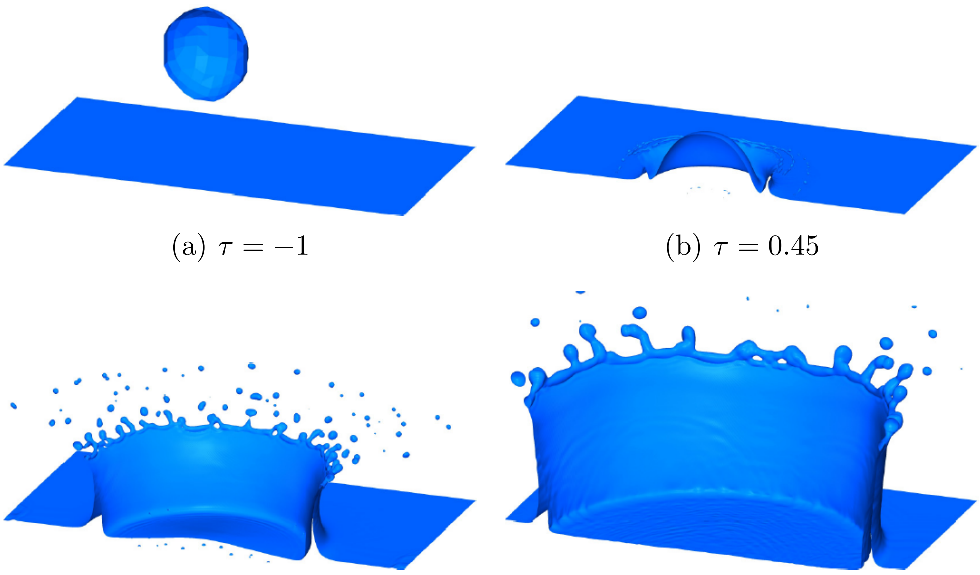

(a) $\tau = -1$ (b) $\tau = 0.45$

(c) $\tau = 1.45$ (d) $\tau = 3.7$

Fig. 5. Numerical simulation, case C (Refinement level 4).

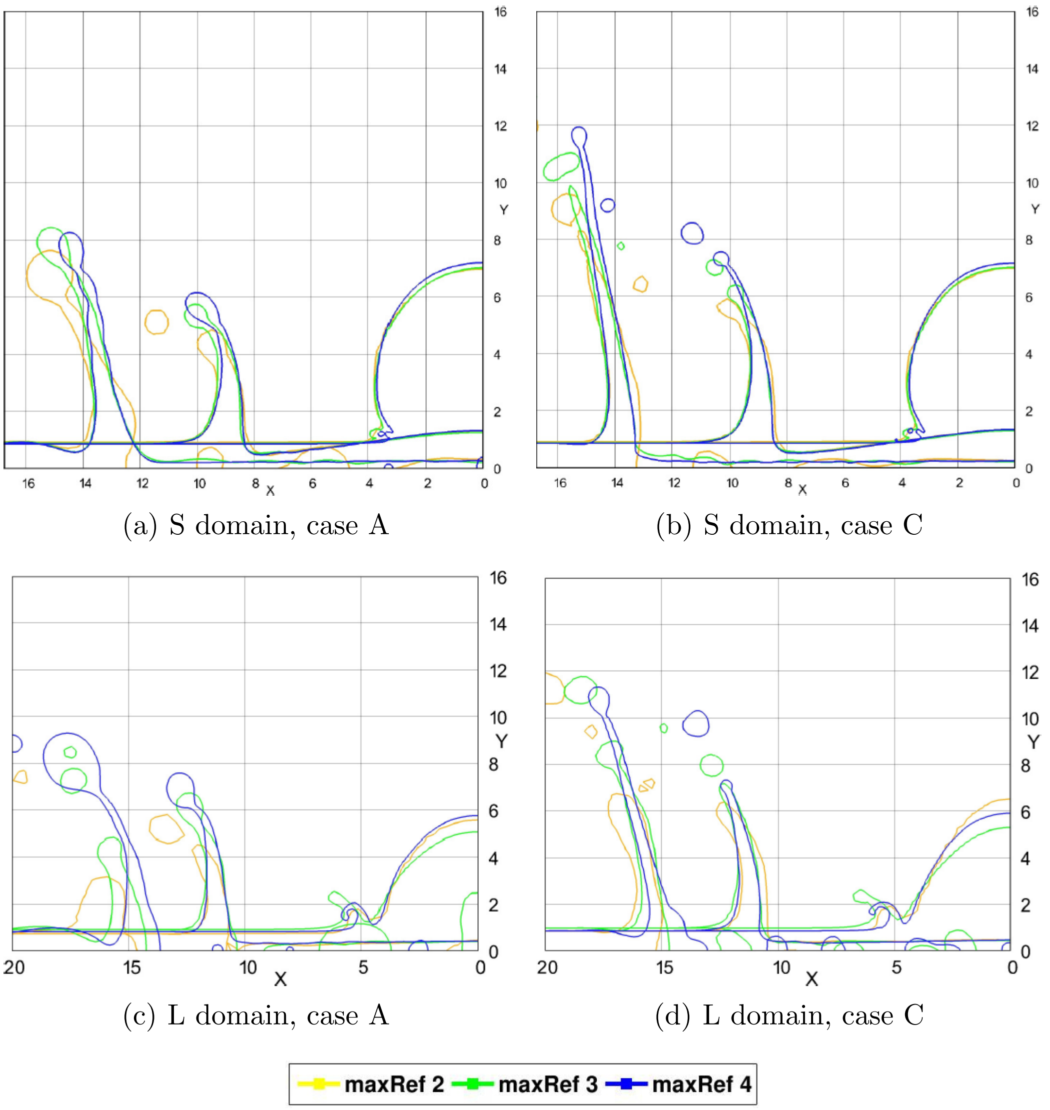

(a) S domain, case A

(b) S domain, case C

(c) L domain, case A

(d) L domain, case C

Fig. 6. Vertical cross sections of splashing lamella. S geometry: $\tau = 0.2, 1.5, 3.5$. L geometry: $\tau = 0.5, 2.5, 5.5$.

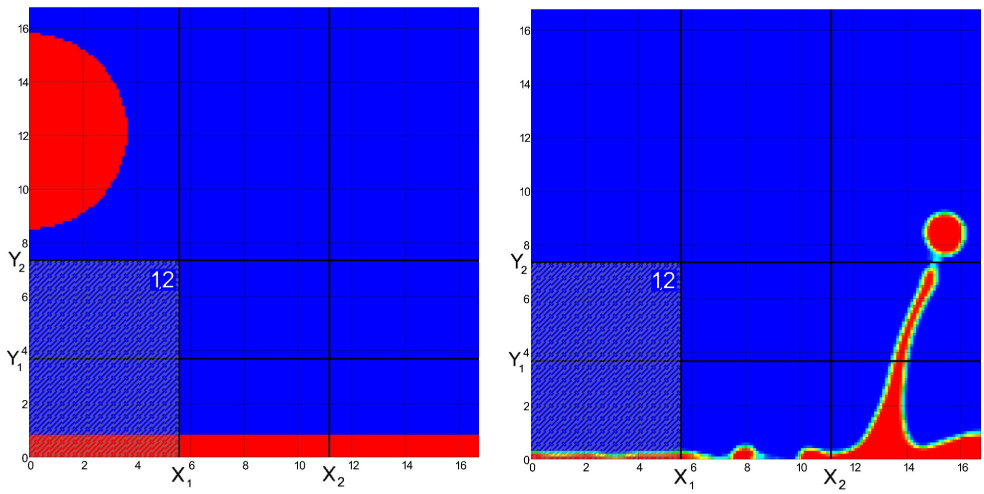

(a) Bounding box (1,2), pre-impact. (b) Bounding box (1,2), post-impact.

Fig. 7. Exemplary pre- and post-impact flow liquid fraction within the bounding box subdivision. Bounding box (1,2) is shaded and it initially contains only a portion of the film; at later time, the liquid content in (1,2) is reduced (cf. figures 8 and 9).

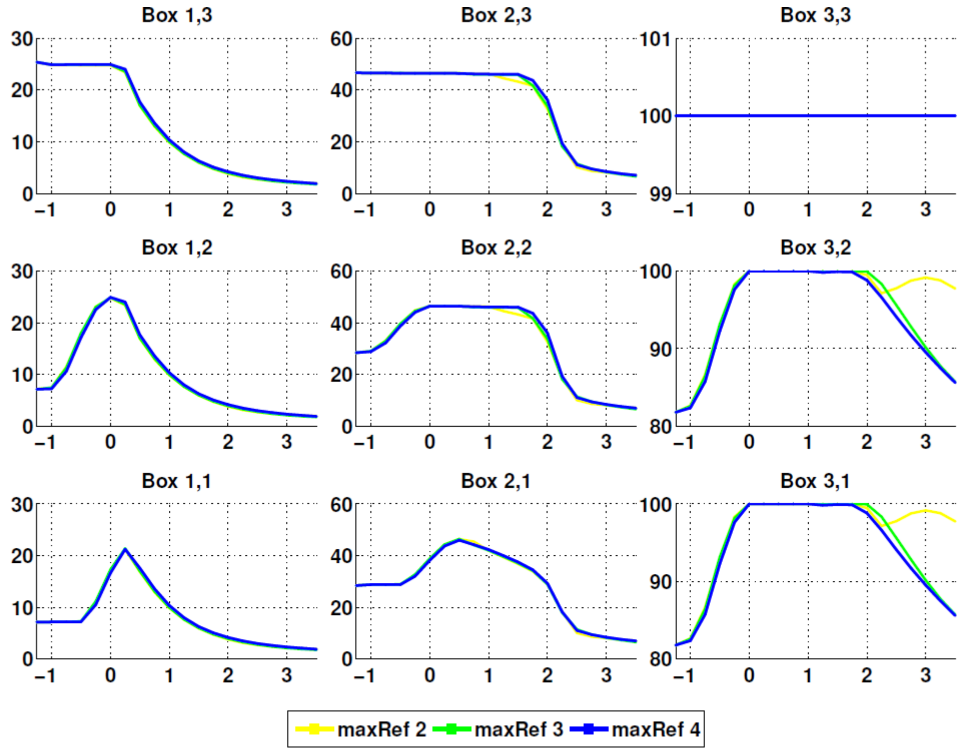

(a) S domain, case A

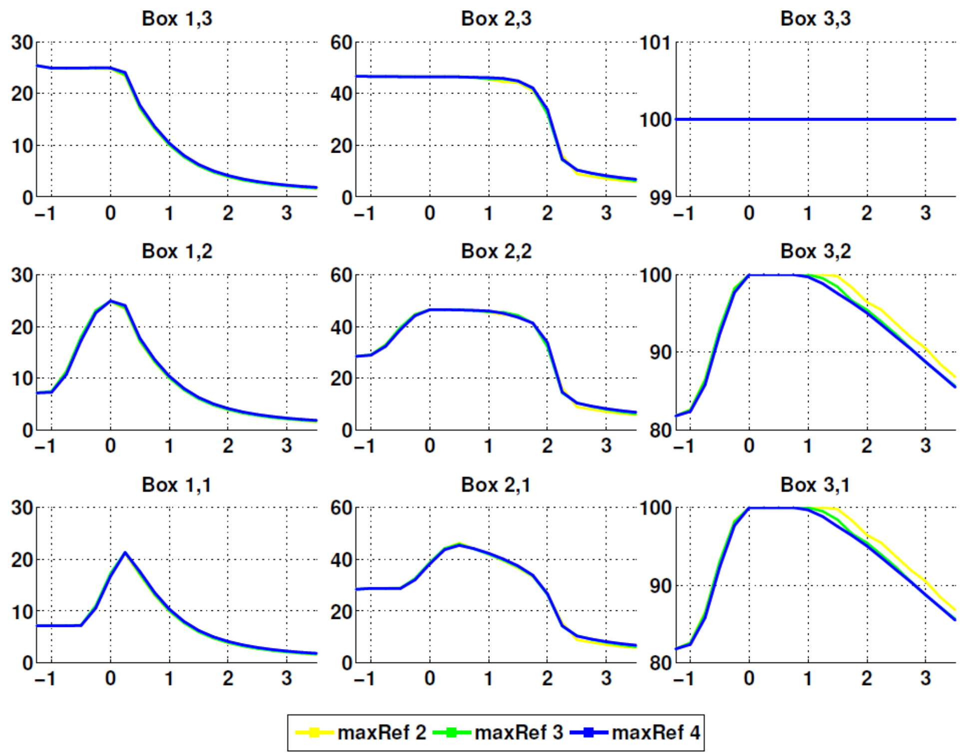

(b) S domain, case C

Fig. 8. S geometry: liquid volume fraction in each bounding box at all times.

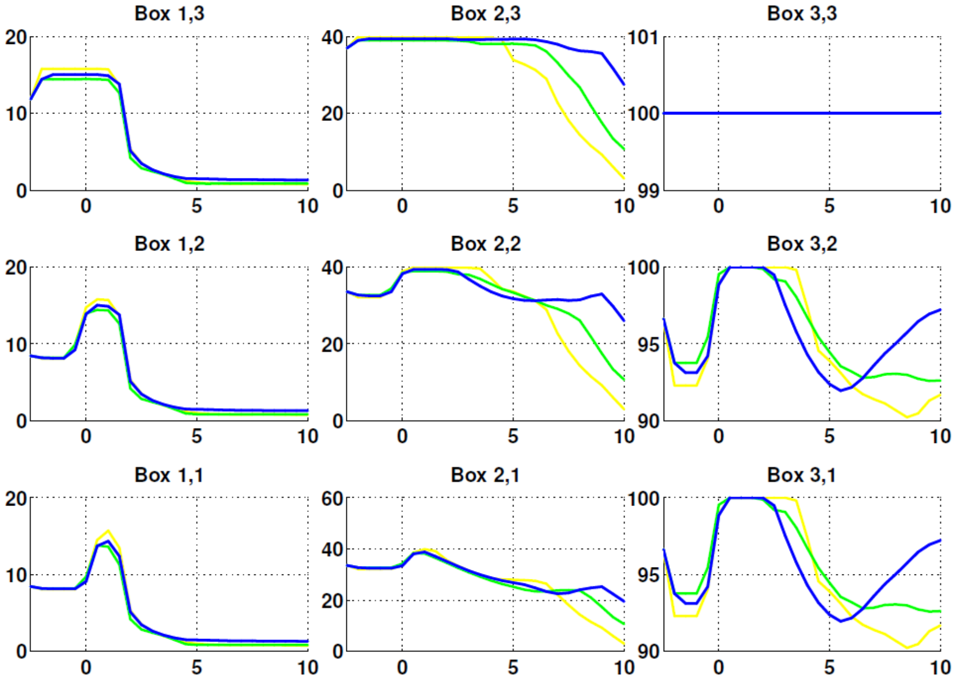

(a) L domain, case A

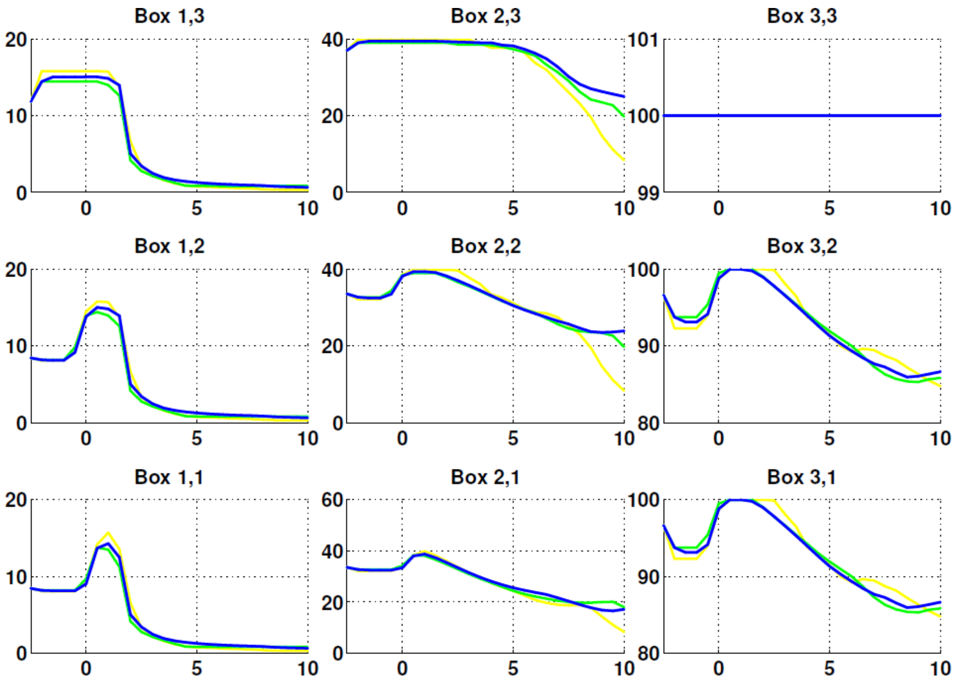

(b) L domain, case C

Fig. 9. L geometry: liquid volume fraction in each bounding box at all times.

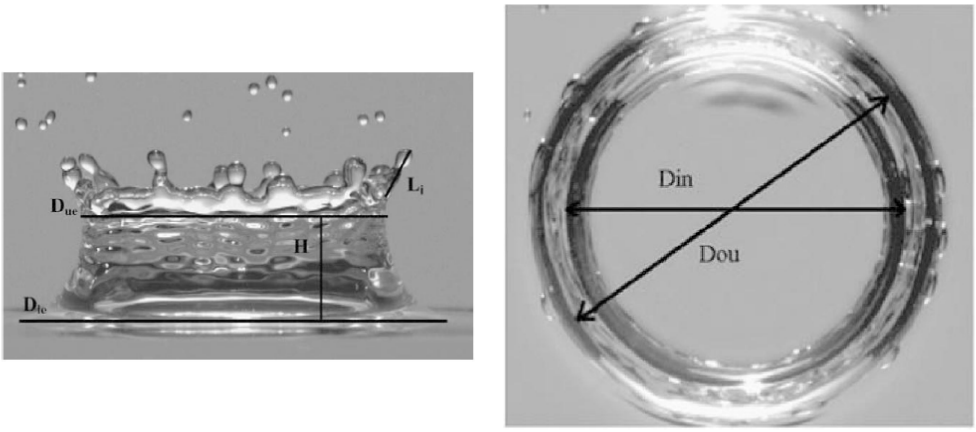

Fig. 10. Graphic definition of the geometrical quantities considered. Images are Figure 1 and Figure 4(a) of Cossali et al. [2].

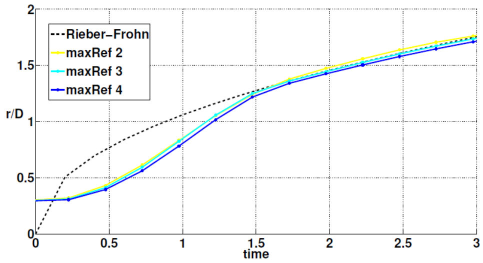

(a) S geometry, case A

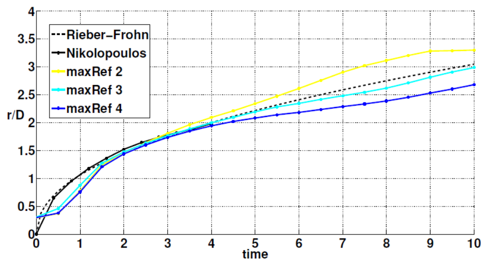

(b) L geometry, case A

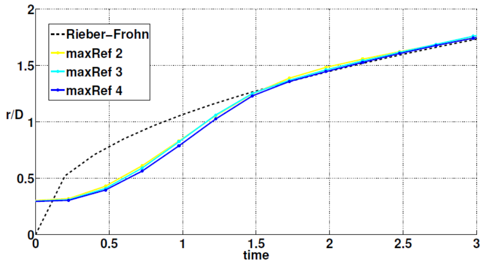

(c) S geometry, case C

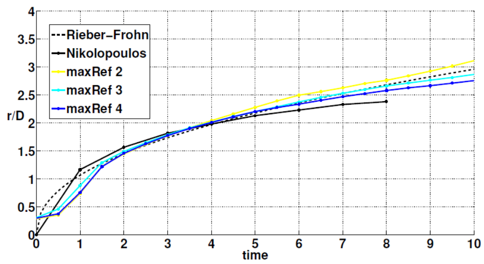

(d) L geometry, case C

Fig. 11. Radius of the crown as a function of time. Comparison between present, Rieber and Frohn's and Nikolopoulos et al.'s results.

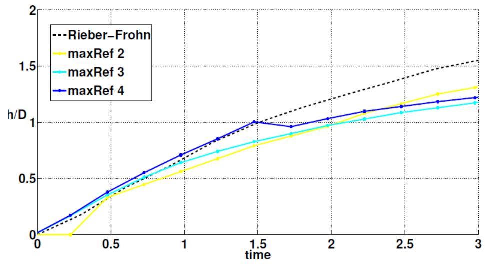

(a) S geometry, case A

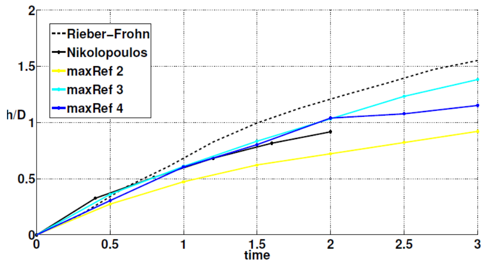

(b) L geometry, case A

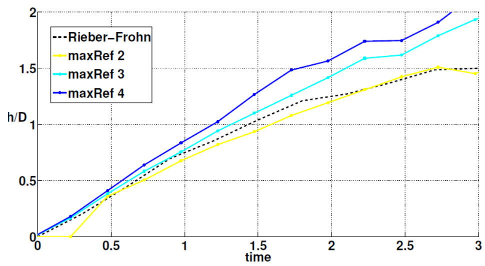

(c) S geometry, case C

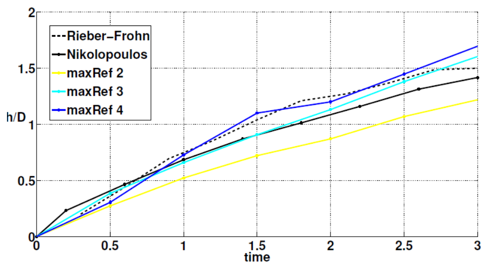

(d) L geometry, case C

Fig. 12. Height of the crown as a function of time. Comparison between present, Rieber and Frohn's and Nikolopoulos et al.'s results.

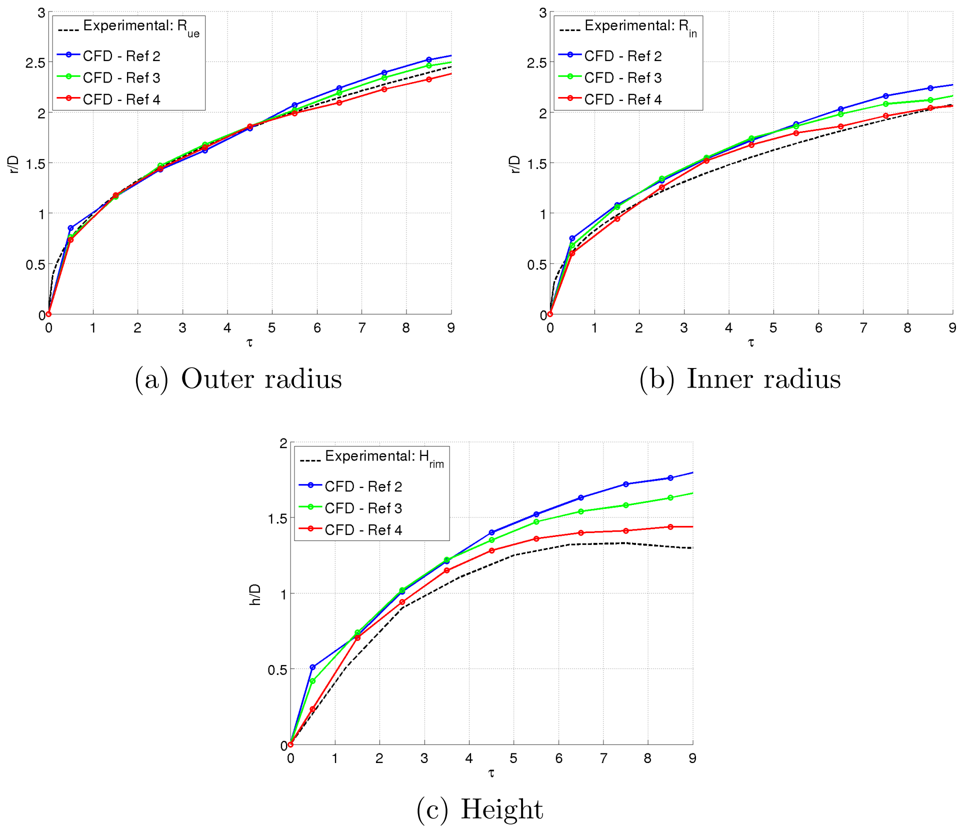

Fig. 13. Comparison to the experimental results in Cossali et al. [2]: outer radius, inner radius and height of the crown.